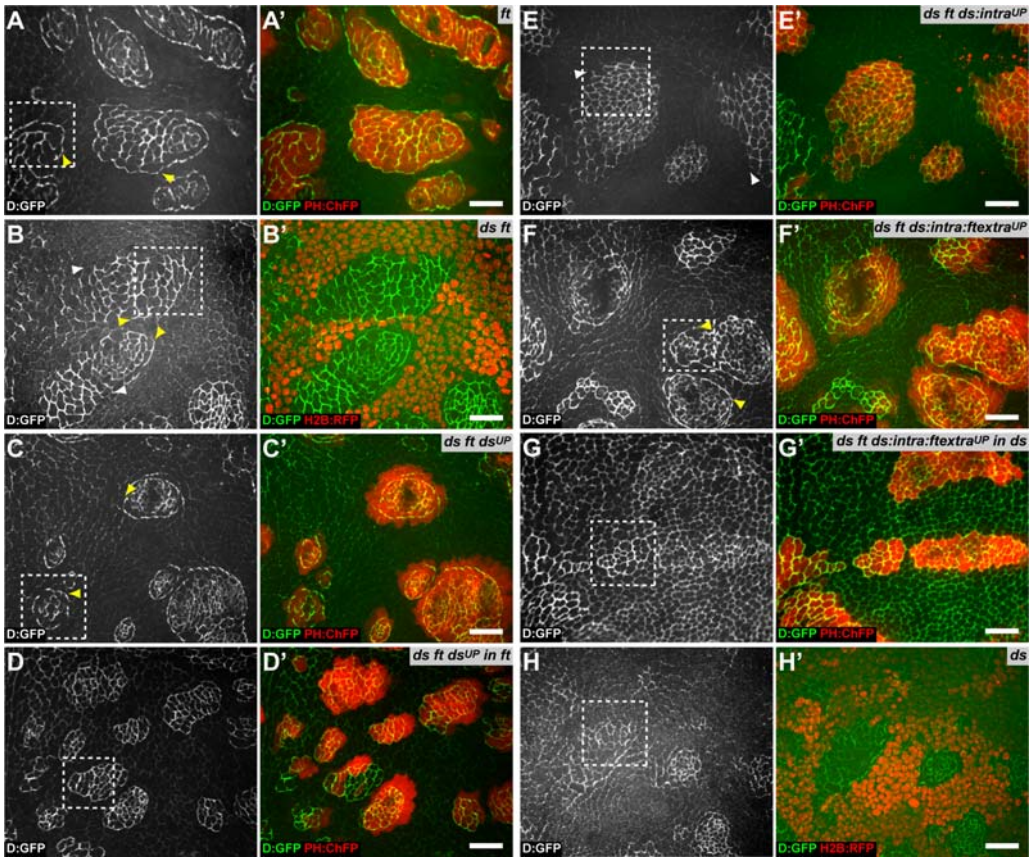

Fig. S1. D:GFP localization in mutant clones and tissues.

(**A-H'**) Confocal images of the localization of D:GFP in clones and tissues of the indicated genotypes. Anterior is to the right. Yellow arrowheads point at cells where D:GFP is polarized whereas white arrowheads indicate the ones which do not harbor polarization. Clones were identified by the absence of H2B:RFP nuclear marker (B', H') or by the presence of the PH:ChFP membrane marker (A', C'-G'). Boxed regions indicate the regions of the clone that are magnified in Fig. 2.

Genotypes are:

S1A : *hs-flp[22]; tub-Gal80[LL10], FRT40A/ ft[Gr-v], FRT40A; tub-Gal4[LL4], UAS-PH:ChFP*

S1B : *hs-flp[22]; ubi-H2B:RFP, FRT40A/ ds[05142], ft[Gr-v], FRT40A; D:GFP*

S1C : *hs-flp[22]; tub-Gal80[LL10], FRT40A/ ds[05142], ft[Gr-v], FRT40A; UAS-ds, D:GFP/ tub-Gal4[LL4], UAS-PH:ChFP*

S1D : *hs-flp[22]; ft[1], tub-Gal80[LL10], FRT40A/ ds[05142], ft[Gr-v], FRT40A; UAS-ds, D:GFP/ tub-Gal4[LL4], UAS-PH:ChFP*

S1E : *hs-flp[22]; tub-Gal80[LL10], FRT40A/ ds[05142], ft[Gr-v], FRT40A; UAS-ds:intra, D:GFP/ tub-Gal4[LL4], UAS-PH:ChFP*

S1F : *hs-flp[22]; tub-Gal80[LL10], FRT40A/ ds[05142], ft[Gr-v], FRT40A; UAS-ds:intra:ft:extra, D:GFP/ tub-Gal4[LL4], UAS-PH:ChFP*

S1G : *hs-flp[22]; ds[05142], tub-gal80[LL10], FRT40A/ ds[05142], ft[Gr-v], FRT40A; UAS-ds:intra:ft:extra, D:GFP/ tub-Gal4[LL4], UAS-PH:ChFP*

S1H : *hs-flp[22]; ubi-H2B:RFP, FRT40A/ ds[05142], FRT40A; D:GFP*

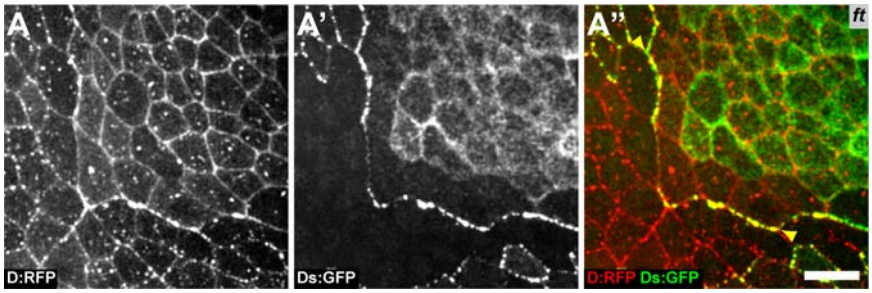

Fig. S2. Ds:GFP and D:RFP localization in *ft* clones.

(**A-A"**) Image of a *ft* clone in a tissue expressing D:RFP (white in A, red in A") and Ds:GFP (white in A', green in A"). Ds:GFP and D:RFP are polarized at the clone boundary (yellow arrowheads). Ds:GFP localization within the clone is more diffuse while D:RFP is still localized at cell-cell junctions. Previous results showed that Dachs membrane localization requires the DHHC palmitoyltransferase Approximated (Matakatsu and Blair, 2008). Therefore our findings suggest that while Ds is necessary to polarize the Dachs myosin, Ds is not required to target Dachs to the cell membrane. Note that the tissue neighboring the *ft* clone does not express Ds:GFP. Since the *ft*, *ds* and *ds:GFP* locus are one the same chromosome arm (2L), the generation of *ft ds:GFP* clones (*hs-flp[22]; FRT40A/ ds:GFP[44.2], ft[Gr-v], FRT40A; D:RFP*) results in a twin clone composed of wt cells (Ds:GFP negative cells). *ft* clones were identified by the increased expression of D:RFP, their circularity and the diffuse Ds:GFP localization. To illustrate the Ds polarization at the *ft* clone boundary we purposely show the boundary between *ft* cells and their wt Ds:GFP negative twins.
Scale bar: 10 µm.

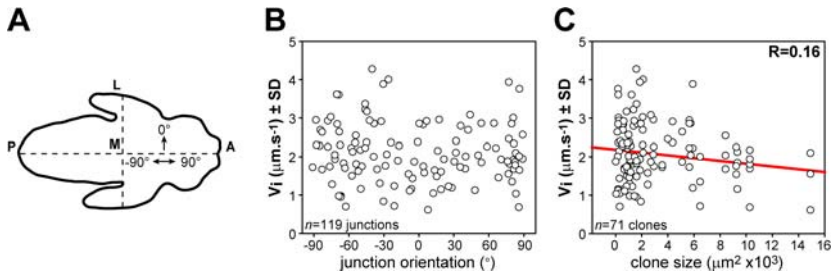

Fig. S3. *ft* clone boundary junction tension is independent of clone size and junction orientation.

(**A**) Sketch of a *Drosophila* pupa. Anterior-posterior (A-P) and medial-lateral axes (M-L) are indicated.

(**B**) Graph of the mean initial recoil velocity of vertices of ablated cell junctions at *ft* clone boundaries versus the orientation of the junction relative to the M-L axis (see panel A).

(**C**) Graph of the mean initial recoil velocity of vertices of ablated cell junctions at *ft* clone boundaries versus the clone size. The correlation score R is 0.16.

For graphs B and C the same data are plotted (119 ablations obtained from 71 different clones).

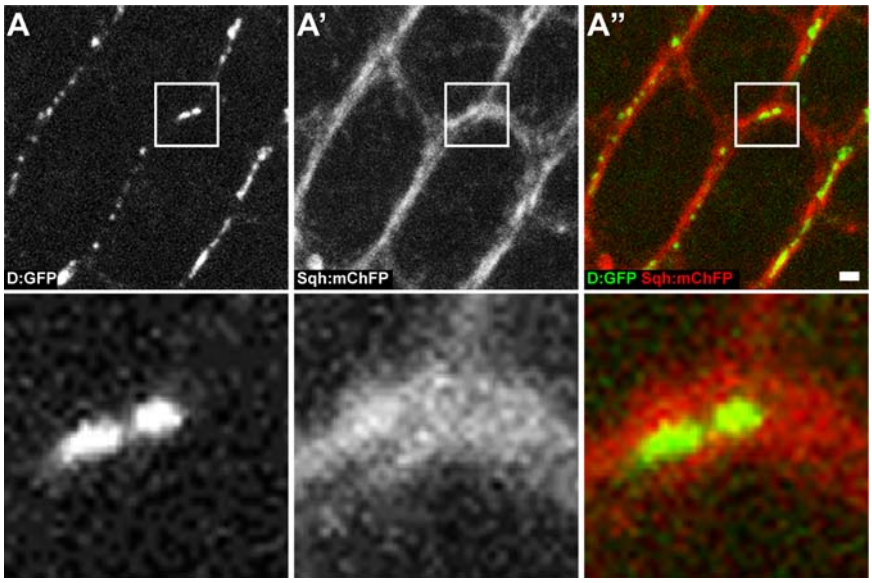

Fig. S4. Dachs myosin localizes in small clusters that do not colocalize with cortical MyoII.

(**A-A"**) Image of a tissue expressing D:GFP (white in A, green in A") and Sqh:mChFP (white in A', red in A"). The lower panels are magnifications of the boxed region. The images demonstrate that D:GFP localizes in small punctate structures at the cell membrane which do not colocalize with the cortical network of MyoII (Sqh:mChFP).

Scale bar: 1 μm.

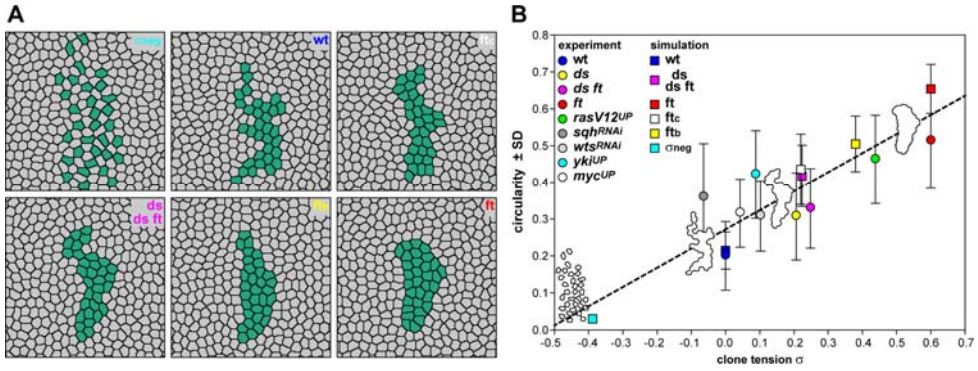

Fig. S5. Junction tensions at clone boundaries and inside clones contribute to clone rounding.

(**A**) Final shapes of six simulated mutant clones; from top left to bottom right: σ_{neg}; wt; ft_c; ds or ds ft; ft_b and ft. Simulated mutant conditions have been sorted in ascending order of their clone tension **σ**, which also corresponds to the ascending order of their final clone circularity (see panel B). In each simulation, the experimentally measured tension ratios γ_b/γ and γ_c/γ were used (see Supplementary Material). Simulating ft clones with junction tension solely reduced inside (ft_c), or solely increased at the clone boundary (ft_b) show that both effects are sufficient to induce clone rounding (the effect of the boundary tension being stronger), and when combined (ft) both contributions add up to achieve a stronger clone rounding. In the first panel (σ_{neg}), the clone tension is negative ($\sigma = -0.39$), illustrating a condition associated with clone scattering. This negative clone tension results from the swapping of γ_c and γ_b measured on *ft* clones, thus illustrating the respective role of γ_c and γ_b.

(**B**) Diagram showing the mean clone circularities C in the different experimental (circles) or simulation (squares) conditions versus dimensionless clone tension parameter σ. For each condition, 20 simulations were performed and thus 20 clones were quantified. Although there is no simple relationship between C and σ, two limits can nevertheless be considered: (i) for σ very large and positive, we expect C to get asymptotically closer to 1, corresponding to a perfectly circular clone; (ii) for σ very large and negative, we expect C to get closer to C_{min}, the latter being a threshold corresponding to the clone cells being completely scattered in the wt tissue ($C_{min} \approx 0.03$ from our ft[inv] simulation resulting in scattered clone). Nevertheless, for σ in the range 0 to 0.5, the circularity C seems to depend rather linearly on σ. We therefore add a linear fit of the experimental and simulated points plotted as a guide for the eye (dotted line): circularity $C \sim 0.5*(\sigma + 0.5)$. Some clone outlines obtained in (A) are added on the graph to illustrate the circularity of clones.

Movie 1. Time-lapse imaging of *ft*^{RNAi} clone.

The behavior of a *ft*^{RNAi} clone within the *Drosophila* anterior notum tissue recorded with 10 min intervals over a period of 30 h. Every cell of the tissue expresses Baz:mChFP (white, left panel and red, right panel) and D:GFP (white, middle panel and green, right panel), while the *ft*^{RNAi} cells also express PH-ChFP (white, left panel and red, right panel). The *ft*^{RNAi} clone accumulates D:GFP and rounds up.

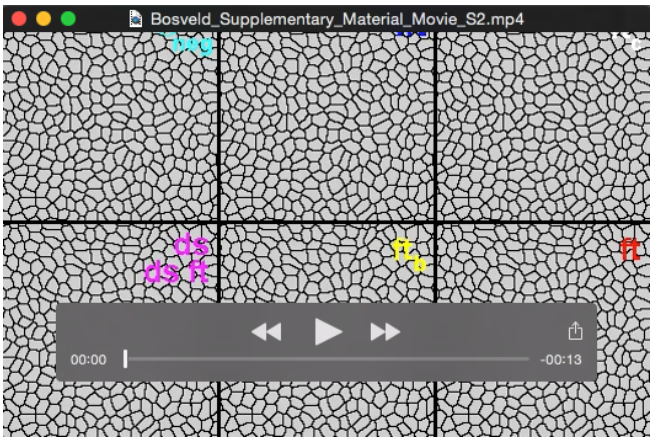

Movie 2: **Simulations showing the evolutions of six clones having different values of clone tension σ.**

Movies showing one simulation in each simulated mutant condition; from top left to bottom right: σ_{neg} (simulating hypothetical clones with inner tension γ_c and boundary tension γ_b respectively higher and lower than wt junction tension $\gamma_b < \gamma < \gamma_c$, namely $\gamma_b < \gamma < \gamma_c$, which results in negative a clone tension σ = -0.39, thereby illustrating a situation inverted with respect to our observed experimental *ft* and *ds*/*ds ft* clones where $\gamma_c < \gamma < \gamma_b$), wt, ft_c (simulating *ft* clones with junction tension solely reduced inside), ds or ds ft, ft_b (simulating *ft* clones with junction tension solely increased at the clone boundary) and ft. Simulated mutant conditions have been sorted in ascending order of their clone tensions **σ**, which also corresponds to the ascending order of their final clone circularities (supplementary material Fig. S5). In each simulation, the experimentally measured tension ratios γ_b/γ and γ_c/γ were used. Importantly, it is possible to run the exact same simulation up to the point where green cells with different junction properties appear, hence the identical initial clone shape in all six simulations (see supplementary movie). This is illustrated by reducing the frame rate of the movie at the time of appearance of the green cells. We mimicked the loss of activity of a given gene by suddenly modifying cell tensions in a group of cells (hence the appearance of green cells), arising from a same mother cell initially placed at the cluster center. The time of this modification was 9000 MCS, roughly corresponding to cells dividing three times to take into account the perdurance of the gene function. After the appearance of green cells, each clone evolves differently according to its own junction properties and clone tension σ, resulting in different final clone circularities. Because of the similarities of the γ_b values measured in *ds* and *ds ft* clones as well as the similarities of γ_c, their means were used for ds and ds ft simulations. As observed in the experiments (Fig. 1B), the shape of cells does not significantly change between the different simulations and clone rounding occurs via cell rearrangements. For each condition, 20 simulations were made and analysed to study clone circularity *in silico*.

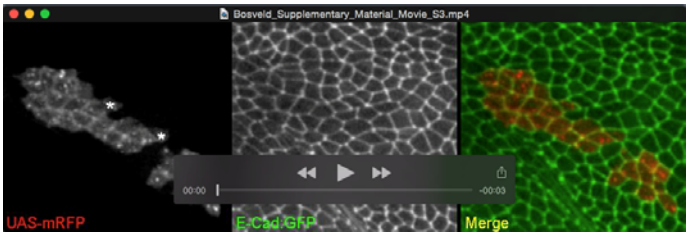

Movie 3: **Time-lapse imaging of *rasV12^{UP}* clone.**

The behavior of a *rasV12^{UP}* clone within the *Drosophila* anterior notum tissue recorded with 10 min intervals over a period of 17 h. The clone expresses mRFP (white, left panel and red, right panel), while every cell of the tissue expresses E-Cad:GFP (white, middle panel and green, right panel). The *rasV12^{UP}* clone rounds up in time. Note that some pI cells, which give rise to microchaetae (asterisks), segregate from the remaining of the clone via cell rearrangements.

Code availability

The code used for simulations based on the cellular Potts model is provided here as a zip file along with the procedure to install and run it on MacOS.

Click here to Download the zip

Supplementary Materials and Methods

Gal4/Gal80^{ts} gated clonal induction and imaging

Unless otherwise stated, somatic clones were induced in the second instar larval stage by heat shock (20 min at 37°C) and analyzed 3-4 days after clone induction in 18-22 hAPF pupae. The behavior of ft^{RNAi} somatic clones was analyzed in *hs-flp; ft$^{[G\text{-}rv]}$, tub-GAL80$^{[ts]}$/ AyGAL4; D:GFP, Baz:mChFP/ UAS-ft$^{[RNAi,\ JF03245]}$, UAS-PH:ChFP* and the behavior of *rasV12* gain of function clones in *hs-flp; UAS-ras$^{[V12]}$/ E-Cad:GFP, tub-GAL80$^{[ts]}$; tub-FRT-GAL80-FRT-GAL4, UAS-mRFP*. Clone induction and temperature changes were performed as follows. Embryos and larvae were raised at 18°C for 7 days. Upon a 7 min heat-shock at 37°C, which is sufficient to create one clone per hemi-notum, the second instar larvae were returned to 18°C. After 4-5 additional days at 18°C, late third instar larvae were transferred to 29°C to induce the expression of the *ft dsRNA*. After 22 ± 4 h at 29°C, the 10 hAPF old pupa were collected, mounted and imaged. Pupae harboring clones of 25-50 cells were selected and imaged for a period of 20-30 h at 29°C. Their behaviors were compared to control clones: groups of 25-50 cells, with a circularity similar to the ones of ft^{RNAi} or $rasV12^{UP}$ clones at the onset of pupariation (10 hAPF), were tracked in a region of the epithelial tissue devoid of ft^{RNAi} clones ($n = 4$) or in E-Cad:GFP pupae filmed at 29°C ($n = 4$). Clones were analyzed in the anterior region of the notum where the Ds and Fj gradients are absent and where cells undergo only one round of cell division (Bosveld et al., 2012).

Theoretical analysis of clone circularity

Theoretical analysis and numerical simulations are inspired by (Graner and Glazier, 1992;Graner, 1993;Bardet et al., 2013) that we adapt here for our specific questions. Several epithelial cellular organizations in *Drosophila* embryo, pupal wing and retina have been successfully described by minimizing an energy that balances adhesion between cells, cortex contractility and volume conservation (for review Morelli et al., 2012). Here, for simplicity, we consider the following energy to describe our 2D epithelium:

$$E = \sum_{\text{sides ij}} \gamma_{ij} l_{ij} + \sum_{\text{cells i}} \kappa_i (a_i - a_i^o)^2 \quad (1)$$

where γ_{ij} and l_{ij} are the line tension and length of the cell junction ij, respectively; κ_i is the compression modulus of cell i ensuring its volume conservation, namely that its area a_i remains close to its target value a_i^o. Note that the energy E displays only two terms: the first one, which can be experimentally probed by laser ablations of junctions, lumps all terms of different origins (adhesion, cortical contractility…) contributing to the full theoretical expression of cell junction tension (Käfer et al., 2007;Lecuit and Lenne, 2007;Rauzi et al., 2008;Hilgenfeldt et al., 2008;Bardet et al., 2013). We

observe that cell junctions are contractile, namely $\gamma_{ij} > 0$, and that the variability of their tensions is low. Their shrinkage is limited by area conservation described by the second term.

Here, we are interested in epithelia displaying two cell types, typically a clone of several mutant cells with different genetic and mechanical properties with respect to wt cells, surrounded by wt tissue, which constitutes our reference state of the tissue. We note γ the junction tension in the wt tissue, γ_c in the mutant clone, γ_b in junctions making up the interface boundary between wt and mutant cells. For simplicity we consider a tissue without boundary (e.g. with periodic boundary conditions), but what follows is readily generalizable to cells surrounded by a medium. Let us break down the energy E according to the two types of homotypic interfaces, and the heterotypic interface:

$$E = \gamma \sum_{ij} l_{ij} + \gamma_b \sum_{ij \in \mathrm{b}} l_{ij} + \gamma_c \sum_{ij \in \mathrm{c}} l_{ij} + \sum_{\text{cells i}} \kappa_i (a_i - a_i^o)^2$$

the first sum being made over wt junctions, the second one over junctions at the clone-wt interface boundary, and the third one over bulk clone junctions. Since we want to study the clone circularity as a function of the difference in cell mechanical properties, we define the perimeter of the clone-wt boundary P_b as $P_b = \sum_{ij \in b} l_{ij}$, and single it out in the energy. The perimeter of a cell reads $p_i = \sum_{<j>} l_{ij}$, the sum being made on cell neighbors. Noticing that $\sum_{\text{sides ij}} l_{ij} = \frac{1}{2} \sum_{\text{cells i}} p_i$, one can rewrite E :

$$E = \frac{\gamma}{2} \sum_i p_i + \frac{\gamma_c}{2} \sum_{i \in c} p_i + \tilde{\sigma} P_b + \sum_{\text{cells i}} \kappa_i (a_i - a_i^o)^2 \qquad \text{with} \qquad \tilde{\sigma} = \gamma_b - \frac{\gamma + \gamma_c}{2}$$

The two first terms are sums of perimeters over *all* cells in the wt tissue and *all* mutant cells in the clone, respectively, including those at the clone boundary. The third term, $\tilde{\sigma} P_b$, directly involves the clone perimeter P_b multiplied by $\tilde{\sigma}$, the difference between the heterotypic junction tension γ_b and the average of the two homotypic junction tensions γ, γ_c. This parameter represents the energy cost associated with the length of the clone boundary when junction tensions $(\gamma, \gamma_b, \gamma_c)$ are different, and vanishes for instance when all junction tensions are the same.

To better understand what $\tilde{\sigma}$ represents, let us consider a change in clone shape and perimeter δP_b that conserves the number of cells and leaves cell areas and perimeters unchanged, namely a change of clone shape only involving cell rearrangements and not changes in cell size and shape, as we observe experimentally. Those cell rearrangements that change clone boundary length P_b convert homotypic junctions into heterotypic junctions and vice versa. The corresponding change in energy then reads:

$$\delta E = \tilde{\sigma}\, \delta P_b$$

Therefore, $\tilde{\sigma} = \partial E / \partial P_b$ represents the energy cost per unit length of increasing the clone boundary length via cell rearrangement, namely the energy cost of turning homotypic junctions from wt and clone tissues into heterotypic boundary junctions. We call it the "clone line tension", not to be confused with the cell junction tension $\gamma_{ij} = \partial E / \partial l_{ij}$ that represents the energy cost per unit length of increasing junction *ij* length and that is probed with laser ablations. The sign and amplitude of $\tilde{\sigma}$ will therefore influence the evolution of the clone boundary toward a state of lower energy satisfying $\delta E < 0$:

$\tilde{\sigma} < 0 \Rightarrow \delta P_b > 0$: increase contact with neighbors favoring clone scattering

$\tilde{\sigma} > 0 \Rightarrow \delta P_b < 0$: decrease contact with neighbors favoring clone rounding

Consequently, taking wt tissue with junction tension γ as a reference, both an increase of junction tension at the clone boundary γ_b, or a decrease of junction tension within the clone γ_c, lead to $\tilde{\sigma} > 0$ and the rounding of the clone. In the last case $\tilde{\sigma} = 0$, which includes the case of a wt clone in a wt tissue, clone shapes have no line tension and their shape is fully determined by other factors. Since the wt tissue is our reference state, and because the initial recoil velocity of vertices of laser-ablated junctions v_{ij}^o measures only relative values of junction tensions ($v_{ij}^o = \mu\gamma_{ij}$, where μ is an unknown prefactor having the dimension of a friction coefficient) (Hutson et al., 2003;Farhadifar et al., 2007;Rauzi et al., 2008), we define the dimensionless clone line tension by $\sigma = \tilde{\sigma} / \gamma$, which reads:

(2) $$\sigma = \frac{1}{\gamma}\left(\gamma_b - \frac{\gamma + \gamma_c}{2}\right)$$

Note that experimental values of σ can therefore be directly estimated for each mutant condition by the ratios of recoil velocities after ablation: $\gamma_k/\gamma = v_k^o/v^o$, with *k* = *b*, *c*. The expression of σ is general and includes the particular case where the tensions on both sides of the clone boundary are the same, namely, $\gamma_c = \gamma$ (Landsberg et al., 2009).

This analysis provides us with qualitative predictions of the resulting clone circularities according to their junction mechanical properties, namely the values of $(\gamma_b/\gamma, \gamma_c/\gamma)$, and ultimately according to σ values.

Numerical simulations of clone circularity

The above simple theoretical analysis provides us with a qualitative trend of the clones to round up $(\sigma > 0)$, or in contrast to scatter $(\sigma < 0)$ according to the sign and amplitude of their dimensionless line tension σ that depends on the ratios $(\gamma_b/\gamma, \gamma_c/\gamma)$ [Eq. (2)]. To go further and actually try to link

more quantitatively the circularity of a growing and proliferating clone to its mechanical properties, we performed numerical simulations based on the energy given in Eq. (1) in a similar way to what was described in (Bardet et al., 2013). They were based on the Cellular Potts Model (CPM), which is relevant to describe variable cell shape, size, packing and irregular fluctuating interfaces (Graner and Glazier, 1992;Glazier and Graner, 1993;Mombach et al., 1995;Käfer et al., 2007;Marée et al., 2007;Krieg et al., 2008;Morelli et al., 2012). Like in experimental images, each cell was defined as a set of pixels, here on a 2D square lattice. The number of pixels defined the cell area, chosen to be comparable with experiments; an area term in the energy constrained this value [Eq. (1)]. We implemented for each cell tension the approximate value of retraction velocity actually measured in experiments, multiplied by 100 to deal with integer numbers for numerical convenience, namely $\gamma = 143, \gamma_b^{\mathrm{ft}} = 200, \gamma_c^{\mathrm{ft}} = 80, \gamma_b^{\mathrm{ds/ds,ft}} = 152, \gamma_c^{\mathrm{ds/ds,ft}} = 97$ and $\gamma_b^{\sigma_{\mathrm{neg}}} = 112, \gamma_c^{\sigma_{\mathrm{neg}}} = 191$. Note that in the simulations, given the very close values of γ_b an γ_c in *ds* and *ds,ft* clones, these two mutant conditions were simulated in a single set of simulations where the averages of γ_b an γ_c over *ds* and *ds,ft* mutant were used. In addition, to study the respective roles of increased clone boundary tension, decreased clone inner tension and their combination in clone rounding, we performed simulations where: (i) only the clone boundary tension was increased to γ_b^{ft} (condition $\mathrm{ft_b}$); (ii) only the clone inner tension was increased to γ_c^{ft} (condition $\mathrm{ft_c}$); (iii) the situation we observe experimentally in ft and ds/ds ft, namely higher clone boundary tension γ_b and lower clone inner tension γ_c was inversed, namely $\gamma_b < \gamma < \gamma_c$ (condition σ_{neg}), leading to a negative value of clone tension σ and clone scattering.

A cell shape changed when one of its pixels became attributed to one of the neighboring cells. The algorithm to minimize the energy *E* used Monte Carlo sampling and the Metropolis algorithm, as follows. We randomly drew (without replacement) a lattice pixel and one of its eight neighboring pixels. If both pixels belonged to different cells, we tried to copy the state of the neighboring pixel to the first one. If the copying decreased *E*, we accepted it, and if it increased *E*, we accepted it with probability $P = \exp(-\Delta E/T)$. Here ΔE was the difference in *E* before and after the considered copying. The prefactor *T* was a fluctuation allowance; it determined the extent of energy-increasing copy events, leading to membrane fluctuations (Mombach et al., 1995;Käfer et al., 2007). It had to be high enough to reduce pinning of the cell junctions on the pixel lattice, and low enough to keep the shape fluctuations close to the experimental ones. A reasonable compromise was obtained when *T* was of order of the junction tensions, and for numerical convenience we chose $T = 100$. We set the compression modulus $\kappa = 1$, and this last parameter could be varied over at least one order of magnitude barely changing the simulation outcomes.

We defined one Monte Carlo time step (MCS) as the number of random drawings equal to the number of lattice pixels. To simulate the growth and proliferation of somatic clones, we doubled the area of each cell over 3000 MCS, then divided it, mimicking the cell cycle which typically lasts 10 h in experiments. In order to mimic the variability of the division times, at the beginning of the simulations all cells were assigned at random a different stage of their cell cycle varying from 0% to 60% of cell cycle completion; and after each division, a random desynchronisation (0% to 20% of cell cycle completion) was introduced. To decrease possible effects of lattice anisotropy on cell shapes, we computed P and ΔE by including interactions up to the 20 next-nearest neighbors (Holm et al., 1991;Käfer et al., 2007).

To avoid possible effects of boundary condition anisotropy on clone shapes, we used periodic boundary conditions. Our field of simulation was a rectangle of 700 x 700 pixels. The cluster of cells was a circle of 700 pixels diameter inscribed in this square. All pixels out of this circle were assigned to external medium: a state without adhesion nor area and perimeter constraints. Cell-medium tension was arbitrarily assigned to $\gamma_0 = 200$ to be comparable with, but larger than, cell-cell tensions, thereby avoiding scattering of cells into the medium. During cluster growth due to rounds of cell growth and division, cells moving outwards and reaching the cluster boundary were transformed into medium. Thus, at each instant, the effective boundary conditions were that of a free circular cluster. Simulated clone images reported here are cropped 171 x 171 pixels zones. They do not exhibit any visible effect of boundary conditions and no direction appears privileged.

Such simulations enable to find a state of mechanical equilibrium of a group of cells that relaxes from an initial configuration of higher energy. Although they do not necessarily accurately describe the actual tissue dynamics leading to this equilibrium state, they are suitable to describe a quasi-static succession of mechanical equilibrium states. This is relevant here, where the cell number and area vary over time scales much slower than the time scale of mechanical relaxation.

We mimicked the loss of activity of a given gene by suddenly modifying cell tensions in a group of cells, arising from a same mother cell initially placed at the cluster center. The time of this modification was 9000 MCS, roughly corresponding to cells dividing three times to take into account the perdurance of the gene function. Although gene function perdurance is difficult to estimate and can vary, we estimated it to roughly 30 h (corresponding to three cell cycles of 10 hours) since in the ft^{RNAi} experiment the increase of D:GFP becomes apparent 30 h after the induction of ft^{RNAi}. For each tested mutant condition, 20 simulations were run with a different choice of the clone mother cell. For the wt, in the same simulation, 20 different mother cells were chosen. Since each simulation started with the

same seed for the random number generator, the only difference between wt and mutant simulations was the change in tension values.

When each cell had divided five times, roughly corresponding to 15000 MCS, we let the system evolve for a few more MCS to reach mechanical equilibrium. In order to compare the experimental and simulation data, the clone circularity was determined using the same method of measurements for experimental and simulated clones. Like in the experiments, we observed that the significant differences in the clone circularity were mainly due to the mutual arrangement of clone cells rather than to cell shape differences.

Table S1. Mutant alleles or transgenes used in this study.

Drosophila stock	Reference or Source
tub-FRT-GAL80-FRT-GAL4 UAS-*mRFP*	Gift from E. Martin-Blanco
E-Cad:GFP	Huang et al., 2009
ubi-*E-Cad:GFP*	Oda et al., 1998
Ds:GFP$^{44.2}$	Brittle et al., 2012
D:GFP	Bosveld et al., 2012
D:RFP	This study
ubi-*Baz:mChFP*	Bosveld et al., 2012
ubi-*H2B:RFP*	Bosveld et al., 2012
sqh-*sqh:GFP*	Royou et al., 2002
sqh-*sqh:ChFP*	Martin et al., 2008
UAS-*ds*	Matakatsu and Blair, 2004
UAS-*ds:intra*	Casal et al., 2006
UAS-*ds:intra:ft:extra*	Casal et al., 2006
dachs^{GC13}	Mao et al., 2006
dachs^{210}	Mao et al., 2006
ft^{1}	Mao et al., 2006
ft^{8}, *dachs*^{GC13}	Mao et al., 2006
ft$^{G\text{-}rv}$	Cho et al., 2006
UAS-*PH:ChFP*	Herszterg et al., 2013
UAS-*yki*	Huang et al., 2005
UAS-*ras*^{V12}	Karim and Rubin, 1998
UAS-*wts*	Feng and Irvine, 2007
hs-*flp*^{22}	Bloomington Stock Center
FRT40A	Bloomington Stock Center
ds^{05142}	Bloomington Stock Center
tub-*GAL4*^{LL4}	Bloomington Stock Center
tub-*GAL80*^{LL10}	Bloomington Stock Center
tub-*GAL80*^{ts10}	Bloomington Stock Center
UAS-*GFP*	Bloomington Stock Center
ubi-*nlsGFP*	Bloomington Stock Center
Act5C-FRT-*yellow*-FRT-*GAL4*^{25}	Bloomington Stock Center
UAS-*ft*$^{RNAi,\ TRiP.JF03245}$	Bloomington Stock Center, Ni et al., 2011
UAS-*dMyc*	Bloomington Stock Center
UAS-*wts*$^{RNAi,\ KK101055}$	VDRC Stock Center, Dietzl et al., 2007
UAS-*sqh*$^{RNAi,\ GD1695}$	VDRC Stock Center, Dietzl et al., 2007

Supplementary References

Bardet, P.L., Guirao, B., Paoletti, C., Serman, F., Léopold, V., Bosveld, F., Goya, Y., Mirouse, V., Graner, F., and Bellaïche, Y. (2013). PTEN Controls Junction Lengthening and Stability during Cell Rearrangement in Epithelial Tissue. Dev Cell *25*, 534-546.

Bosveld, F., Bonnet, I., Guirao, B., Tlili, S., Wang, Z., Petitalot, A., Marchand, R., Bardet, P.L., Marcq, P., et al. (2012). Mechanical Control of Morphogenesis by Fat/Dachsous/Four-Jointed Planar Cell Polarity Pathway. Science *336*, 724-27.

Brittle, A., Thomas, C., and Strutt, D. (2012). Planar polarity specification through asymmetric subcellular localization of Fat and Dachsous. Curr Biol *22*, 907-914.

Casal, J., Lawrence, P.A., and Struhl, G. (2006). Two separate molecular systems, Dachsous/Fat and Starry night/Frizzled, act independently to confer planar cell polarity. Development *133*, 4561-572.

Cho, E., Feng, Y., Rauskolb, C., Maitra, S., Fehon, R., and Irvine, K.D. (2006). Delineation of a Fat tumor suppressor pathway. Nat Genet *38*, 1142-150.

Dietzl, G., Chen, D., Schnorrer, F., Su, K.C., Barinova, Y., Fellner, M., Gasser, B., Kinsey, K., Oppel, S., et al. (2007). A genome-wide transgenic RNAi library for conditional gene inactivation in Drosophila. Nature *448*, 151-56.

Farhadifar, R., Röper, J.C., Aigouy, B., Eaton, S., and Jülicher, F. (2007). The Influence of Cell Mechanics, Cell-Cell Interactions, and Proliferation on Epithelial Packing. Curr Biol *17*, 2095-2104.

Feng, Y., and Irvine, K.D. (2007). Fat and expanded act in parallel to regulate growth through warts. Proc Natl Acad Sci U S A *104*, 20362-67.

Glazier, J.A., and Graner, F. (1993). Simulation of the differential adhesion driven rearrangement of biological cells. Phys Rev E *47*, 2128-154.

Graner, F. (1993). Can surface adhesion drive cell rearrangement? Part I: biological cell-sorting. J theor Biol *164*, 455-476.

Graner, F., and Glazier, J. (1992). Simulation of biological cell sorting using a two-dimensional extended Potts model. Phys Rev Lett *69*, 2013-2016.

Herszterg, S., Leibfried, A., Bosveld, F., Martin, C., and Bellaïche, Y. (2013). Interplay between the Dividing Cell and Its Neighbors Regulates Adherens Junction Formation during Cytokinesis in Epithelial Tissue. Dev Cell *24*, 256-270.

Hilgenfeldt, S., Erisken, S., and Carthew, R.W. (2008). Physical modeling of cell geometric order in an epithelial tissue. Proc Natl Acad Sci U S A *105*, 907.

Holm, E.A., Glazier, J.A., Srolovitz, D.J., and Grest, G.S. (1991). Effects of lattice anisotropy and temperature on domain growth in the two-dimensional Potts model. Phys Rev A *43*, 2662-68.

Huang, J., Wu, S., Barrera, J., Matthews, K., and Pan, D. (2005). The Hippo signaling pathway coordinately regulates cell proliferation and apoptosis by inactivating Yorkie, the Drosophila Homolog of YAP. Cell *122*, 421-434.

Huang, J., Zhou, W., Dong, W., Watson, A.M., and Hong, Y. (2009). Directed, efficient, and versatile modifications of the Drosophila genome by genomic engineering. Proc Natl Acad Sci U S A *106*, 8284-89.

Hutson, M.S., Tokutake, Y., Chang, M.S., Bloor, J.W., Venakides, S., Kiehart, D.P., and Edwards, G.S. (2003). Forces for morphogenesis investigated with laser microsurgery and quantitative modeling. Science *300*, 145-49.

Johnston, C.A., Hirono, K., Prehoda, K.E., and Doe, C.Q. (2009). Identification of an Aurora-A/PinsLINKER/Dlg spindle orientation pathway using induced cell polarity in S2 cells. Cell *138*, 1150-163.

Karim, F.D., and Rubin, G.M. (1998). Ectopic expression of activated Ras1 induces hyperplastic growth and increased cell death in Drosophila imaginal tissues. Development *125*, 1-9.

Käfer, J., Hayashi, T., Marée, A.F., Carthew, R.W., and Graner, F. (2007). Cell adhesion and cortex contractility determine cell patterning in the Drosophila retina. Proc Natl Acad Sci U S A *104*, 18549-554.

Krieg, M., Arboleda-Estudillo, Y., Puech, P.H., Käfer, J., Graner, F., Müller, D.J., and Heisenberg, C.P. (2008). Tensile forces govern germ-layer organization in zebrafish. Nat Cell Biol *10*, 429-436.

Landsberg, K.P., Farhadifar, R., Ranft, J., Umetsu, D., Widmann, T.J., Bittig, T., Said, A., Jülicher, F., and Dahmann, C. (2009). Increased cell bond tension governs cell sorting at the Drosophila anteroposterior compartment boundary. Curr Biol *19*, 1950-55.

Lecuit, T., and Lenne, P.F. (2007). Cell surface mechanics and the control of cell shape, tissue patterns and morphogenesis. Nat Rev Mol Cell Biol *8*, 633-644.

Mao, Y., Rauskolb, C., Cho, E., Hu, W.L., Hayter, H., Minihan, G., Katz, F.N., and Irvine, K.D. (2006). Dachs: an unconventional myosin that functions downstream of Fat to regulate growth, affinity and gene expression in Drosophila. Development *133*, 2539-551.

Marée, A.F.M., Grieneisen, V.A., and Hogeweg, P. (2007). The Cellular Potts Model and Biophysical Properties of Cells, Tissues and Morphogenesis. In Cell Based Models in Biology and Medicine (A.R.A. Anderson, M.A.J. Chaplain, and K.A. Rejniak, Birkhäuser Basel).

Martin, A.C., Kaschube, M., and Wieschaus, E.F. (2009). Pulsed contractions of an actin-myosin network drive apical constriction. Nature *457*, 495-499

Matakatsu, H., and Blair, S.S. (2004). Interactions between Fat and Dachsous and the regulation of planar cell polarity in the Drosophila wing. Development *131*, 3785-794.

Matakatsu, H., and Blair, S.S. (2008). The DHHC palmitoyltransferase approximated regulates Fat signaling and Dachs localization and activity. Curr Biol *18*, 1390-95.

Mombach, J.C., Glazier, J.A., Raphael, R.C., and Zajac, M. (1995). Quantitative comparison between differential adhesion models and cell sorting in the presence and absence of fluctuations. Phys Rev Lett *75*, 2244-47.

Morelli, L.G., Uriu, K., Ares, S., and Oates, A.C. (2012). Computational approaches to developmental patterning. Science *336*, 187-191.

Ni, J.Q., Zhou, R., Czech, B., Liu, L.P., Holderbaum, L., Yang-Zhou, D., Shim, H.S., Tao, R., Handler, D., et al. (2011). A genome-scale shRNA resource for transgenic RNAi in Drosophila. Nat Methods *8*, 405-07.

Oda, H., Tsukita, S., and Takeichi, M. (1998). Dynamic behavior of the cadherin-based cell-cell adhesion system during Drosophila gastrulation. Dev Biol *203*, 435-450.

Rauzi, M., Verant, P., Lecuit, T., and Lenne, P.F. (2008). Nature and anisotropy of cortical forces orienting Drosophila tissue morphogenesis. Nat Cell Biol *10*, 1401-410.

Royou, A., Sullivan, W., and Karess, R. (2002). Cortical recruitment of nonmuscle myosin II in early syncytial Drosophila embryos: its role in nuclear axial expansion and its regulation by Cdc2 activity. J Cell Biol *158*, 127-137.

Ségalen, M., Johnston, C.A., Martin, C.A., Dumortier, J.G., Prehoda, K.E., David, N.B., Doe, C.Q., and Bellaïche, Y. (2010). The Fz-Dsh planar cell polarity pathway induces oriented cell division via Mud/NuMA in Drosophila and zebrafish. Dev Cell *19*, 740-752.